https://doi.org/10.5194/egusphere-2026-1605
Preprint. Discussion started: 15 June 2026


# Assessing Buried Landslide Rupture Surfaces Using Genetic Algorithms and Dynamic Flow Modeling

Hock-Kiet Wong[1, †], Yih-Chin Tai[1], and Ching-Fang Lee[2]

[1]Department of Hydraulic and Ocean Engineering, National Cheng Kung University, No.1, University Road, Tainan, 70101, Taiwan.
[2]InnoFusion Environmental Management Co., LTD, Taipei, Taiwan.
[†]Current address: Department of Marine Environment and Engineering, National Sun Yat-sen University, Kaohsiung, 80424, Taiwan.

**Correspondence:** Yih-Chin Tai (yctai@ncku.edu.tw)

**Abstract.** Estimating the landslide volume and rupture geometry remains a critical challenge, particularly for landslides whose toe of the rupture surface is buried by displaced materials. This geometrical ambiguity leads to significant uncertainties in hazard assessment. To address this issue, this study proposes an integrated framework that couples a geometric search method with a physics-based dynamic model. This study employ the Genetic-Algorithm Ellipse-Referenced Idealized Curved Surface (GA-ER-ICS) to generate candidate rupture surfaces. Unlike traditional geometric fitting, the optimal rupture surface is constrained not only by topographic fit but also by the dynamic behavior of the post-failure motion. The validity of the approximated geometry is verified by simulating the subsequent flow paths and deposition patterns using a GPU-accelerated two-phase grain-fluid model (MoSES_2PDF). The proposed method is validated against the 2009 Hsiaolin landslide and applied to the 2022 Provincial Highway No. 7 landslide event in Taiwan. Results demonstrate that the integrated approach successfully approximates the buried rupture surface, achieving a deposition coverage accuracy of over 75% and reducing the uncertainty in volume estimation compared with the estimates derived from the difference between pre- and post-event Digital Elevation Models (DEMs). This study highlights the potential of using dynamic flow calibration to resolve static geometric indeterminacy in back-calculation of the landslide failure surface.

## 1 Introduction

In mountainous regions globally, large-scale landslides pose severe threats to human settlements and infrastructure. Landslide propagation is often triggered by events such as increased pore pressure due to rainfall, snowmelt, earthquakes, or human activities, which decrease the stability of surface materials (e.g., Terzaghi, 1950; Jaboyedoff et al., 2018). For effective hazard mitigation and the establishment of early warning systems, a timely and reliable assessment of the potential landslide volume is paramount. The magnitude of the mobilized mass is not merely a statistical figure; it is the governing factor that dictates the flow hydrodynamics, including runout distance, flow velocity, and the extent of the impact area (Legros et al., 2000; Hsu, 1975). This indicates that landslide volume plays a critical role in estimating landslide magnitude, especially for rotational and translational landslides where the toe of the surface of rupture is buried, making volume estimation challenging and uncer-

https://doi.org/10.5194/egusphere-2026-1605
Preprint. Discussion started: 15 June 2026


tain (Varnes, 1978; Hungr et al., 2014). Previous studies have emphasized that for long-runout landslides, the volume of the displaced material is often more critical than the elevation difference between the scarp and the deposition zone in determining the catastrophic potential (Scheidegger, 1973; Legros et al., 2000). Furthermore, accurate volume estimation is essential for analyzing secondary hazards, such as the formation of landslide dams or the obstruction of river channels (Corominas, 1996; Jakob, 2005; Jakob et al., 2012; von Ruette et al., 2016). Consequently, any uncertainty in the initial volume estimation propagates through the entire hazard assessment chain, potentially leading to inadequate engineering designs or underestimated risk zones (Jaboyedoff et al., 2020).

Despite the importance of accurate volume quantification, it remains a challenging task in post-event investigations, particularly for rotational and translational landslides. A fundamental difficulty arises when the toe of the surface of rupture is buried by the displaced material. In such scenarios, the observable topography represents the final depositional surface rather than the actual slip surface. Traditional approaches, which rely on the difference between pre- and post-event Digital Elevation Models (DEMs), which often referred to as the Difference of DEMs (DoD), can only provide the net volume change (erosion minus deposition). They fail to distinguish the boundary between the landslide scarp and the debris flow endangered area (Travelletti et al., 2014; Tang et al., 2020). This "blind zone" at the toe introduces a high degree of geometric ambiguity, as infinite potential rupture surfaces could theoretically connect the visible scarp to an unknown point beneath the deposit (illustrated in Figure 1). This indeterminacy is the primary source of uncertainty in constructing landslide inventories and calibrating numerical models.

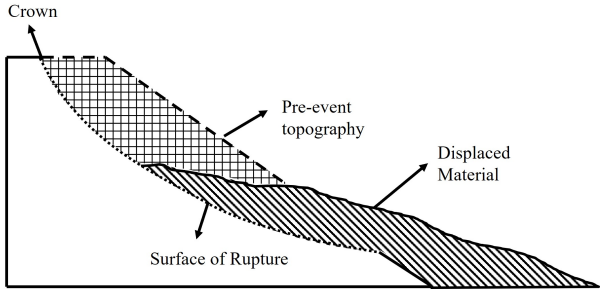


**Figure 1.** Schematic cross-section showing the relationship between the pre-event topography, the rupture surface, and the final distribution of the displaced mass.

To address the problem of estimating the rupture surface, various methodologies have been proposed. Geometrical approaches, such as the Sloping Local Base Level (SLBL) (Jaboyedoff et al., 2012), Smooth Minimal Surfaces Method (SMS) (Kuo et al., 2020) and spline-based surface fitting (Tang et al., 2020), attempt to interpolate the missing geometry based on surface curvature and geomorphological continuity. While computationally efficient, these methods often produce surfaces that are geometrically smooth but may lack geological realism. On the other hand, limit equilibrium methods (LEM), implemented in software such as GeoStudio (GEO-SLOPE, 2021) or Scoops3D (Reid et al., 2015), search for the critical slip surface based on the lowest factor of safety. However, these geotechnical approaches typically require detailed subsurface parameters (e.g., cohesion, friction angle, pore water pressure) which are rarely available in the immediate aftermath of a disaster. More im-

https://doi.org/10.5194/egusphere-2026-1605
Preprint. Discussion started: 15 June 2026


**Table 1.** Comparison of existing approaches for landslide rupture-surface and volume estimation. The present study introduces dynamic post-failure kinematics as an additional inverse constraint.

| Method | Category | Primary input | Output | Key limitation |
|---|---|---|---|---|
| SLBL | Geometric | Scarp boundary | Slip surface | Geometry only; no dynamics |
| SMS | Geometric | Scarp + volume | Smooth minimal surface | Clear delineation is required |
| Spline fitting | Geometric | Erosion control points | Polynomial surface | No kinematic verification |
| LEM | Geotechnical | Geological parameters | Critical slip surface | Subsurface data is required |
| Present study | Geometric + Dynamic | Pre/post DEMs, orthophoto | Rupture surface + verified runout | Deviations from the delineated area |

portantly, both geometrical and stability-based methods largely operate under static constraints. They reconstruct the failure surface based on the initiation phase but ignore the subsequent dynamic process. However, one of the critical questions appears to be missing: "If the landslide failed along this approximated surface, would the resulting debris actually travel to the observed deposition location?" This disconnect between the approximated geometry and the post-failure kinematics leads to the issue of equifinality, where multiple approximated surfaces may appear plausible but produce vastly different runout behaviors. Once the landslide volume and distribution is known, it can be used to predict sediment movement by integrating hydrological conditions or assuming inflow conditions. Sequence flow-path numerical models include HEC-RAS model (Brunner, 2016), HyperKanako model (Nakatani et al., 2008), RAMMS (RAMMS, 2024) and MoSES_2PDF (Tai et al., 2019). To position the present study within this broader landscape, Table 1 summarizes the principal categories of existing approaches for rupture-surface and landslide-volume estimation, along with their data requirements and key limitations. Whereas purely geometric and limit-equilibrium methods rely on static constraints alone, the present framework is, to the authors' knowledge, among the first to use post-failure kinematics as an inverse constraint on the buried rupture geometry.

To resolve this geometric ambiguity, this study proposes a novel, integrated backward-analysis framework that couples geometric search algorithms with physics-based dynamic modeling. This study hypothesize that the correct rupture surface must satisfy not only geometric constraints (fitting the scarp) but also kinematic constraints (reproducing the deposition pattern). We employ the Genetic-Algorithm Ellipse-Referenced Idealized Curved Surface (GA-ER-ICS) method (Wang et al., 2022; Tai et al., 2020) to efficiently search for optimal rupture geometries. The GA-ER-ICS allows for the rapid generation of candidate surfaces by parameterizing the landslide geometry into an idealized ellipsoidal form, which is particularly suitable for data-scarce regions. To validate these candidates, the geometry is fed into a two-phase grain-fluid model (MoSES_2PDF) (Ko et al., 2021a; Wong et al., 2024). This GPU-accelerated simulation tool computes the flow path and final deposition of the granular-fluid mixture, allowing for a direct comparison with the observed post-event topography. By leveraging the high computational efficiency of GPU architecture, this study performs an iterative optimization where the fitness of a rupture surface is evaluated by the match between the simulated and observed deposits. This approach is validated against the 2009 Hsiaolin landslide and subsequently applied to the 2022 Provincial Highway No. 7 landslide event in Taiwan. The primary contribution of this work is to demonstrate how dynamic flow calibration can significantly reduce the uncertainty in reconstructing buried landslide geometries, providing a robust tool for preliminary hazard assessment.

https://doi.org/10.5194/egusphere-2026-1605
Preprint. Discussion started: 15 June 2026


## 2 Integrated Assessment Framework

To address the challenge of reconstructing a landslide rupture surface with a buried toe, this study employs an integrated framework that couples geometric inversion with dynamic verification. The workflow consists of two primary stages: (1) generating candidate rupture surfaces using the Genetic-Algorithm Ellipse-Referenced Idealized Curved Surface (GA-ER-ICS) method based on varying boundary scenarios; and (2) validating these candidates by simulating the landslide mass movement using a GPU-accelerated two-phase grain-fluid model (MoSES_2PDF).

### 2.1 Geometric Reconstruction: The GA-ER-ICS Framework

The GA-ER-ICS method assumes that the landslide rupture surface can be approximated by a geometrically adaptable idealized curved surface (ICS) (Wang et al., 2022). The geometry of this surface is governed by a reference ellipse projected onto the horizontal plane, which is anchored by four key boundary points ($P_1$ to $P_4$).

Figure 2 depicts the top view (upper panel) and side view (bottom panel) of a failured slope. As shown in the top view, the reference ellipse can be constructed by four points ($P_1$, $P_2$, $P_3$ and $P_4$) on the plausible boundary of the rupture surface in the DEMs. The line $\overline{P_1P_2}$ approximately determines the major axis of the ellipse along the down-slope direction, while the width of the reference ellipse is determined by the minimizing the root mean square (RMS) with respect to points $P_3$ and $P_4$ through iteration. With a depth defined at the center, the ellipse corresponds to a unique ICS (Ko et al., 2021a) and the amount of released mass are specified, the released volume can be estimated either from pre- and post-event DEMs with field investigations, or from empirical "area-volume" relations (e.g., Guzzetti et al., 1999; Larsen et al., 2010; Guzzetti et al., 2008, 2009; Meier et al., 2020). In the searching process, various orientations of the reference ellipse are taken into account. Each reference ellipse corresponds to a unique ICS, resulting in multiple ICS candidates. Using the genetic algorithm, the best-fitted ICS is identified based on assigned condition(s), such as the best fit to the area of the ruptured surface, the distributions of the displaced material (deposit), or the smallest factor of safety. In other words, this GA-ER-ICS method is rather flexible, because it can be used to estimate and approximate the potential surface of rupture based on various assigned conditions.

In the specific cases targeted by this study, the true location of the toe ($P_2$) is obscured by displaced material, introducing geometric indeterminacy. Through the pre- and post-event DEMs, only part of the eroded area (upper part of the rupture surface) and the whole deposit area (extent of the displaced material, indicated by shaded area in Figure 2) can be identified. To resolve this, a scenario-based approach is adopted where $P_1$ is fixed at the identifiable scarp crown, while the location of $P_2$ is treated as a variable. Multiple scenarios are designed by hypothesizing potential locations for $P_2$, ranging from the visible toe of the deposit to the theoretical buried toe of the original slope. As shown in Figure 2(b), several possible locations of $P_2$ are selected from the toe of the original slope toward the crown. In each scenario, the corresponding ICS is constructed with respect to the released volume, generally estimated based on field survey and the difference between the pre- and post-event DEMs. In the GA searching process, the gens are $(\delta x, \delta y, \delta\theta, \delta L_1)$ with range $(\pm 8\Delta x, \pm 8\Delta y, \pm 15°, \pm 8\Delta x)$, where $\Delta x$ and $\Delta y$ stand for the mesh sizes in $x$- and $y$-direction, respectively, and $\theta$ denotes the tilting angle of the reference ellipse. The optimization process is executed over 15 generations with a population of 30 individuals per generation to ensure convergence.

https://doi.org/10.5194/egusphere-2026-1605
Preprint. Discussion started: 15 June 2026


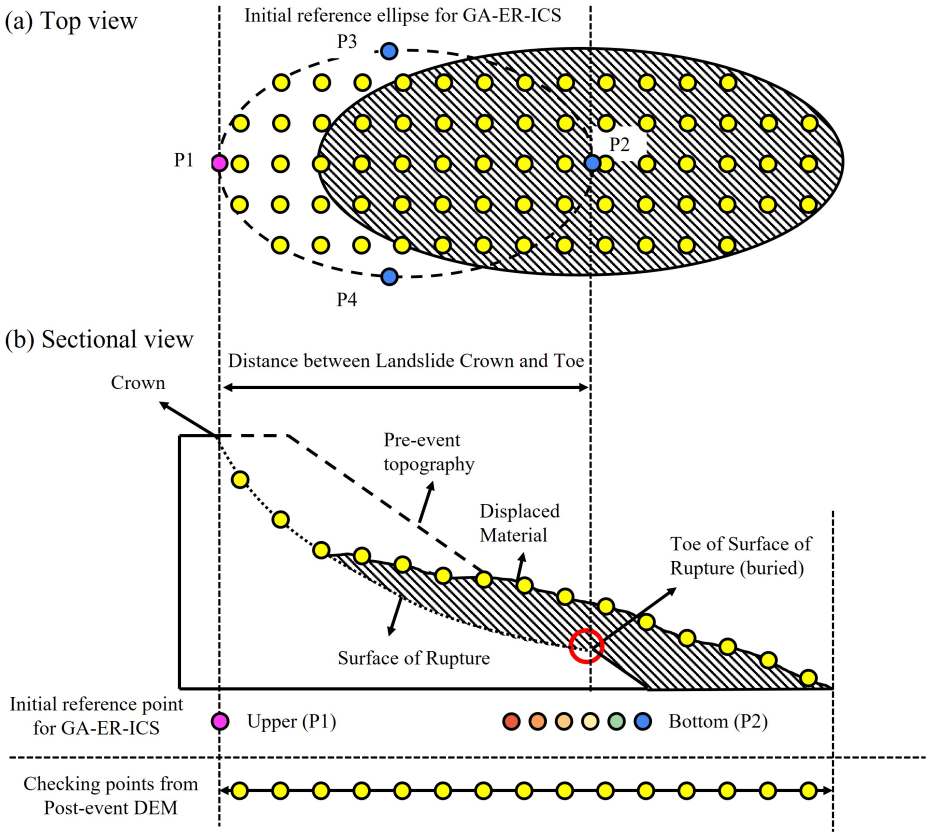


**Figure 2.** Geometric definition and search strategy for the rupture surface reconstruction. (a) Top view showing the parameterization of the reference ellipse and the grid of control points used to calculate the RMS error. (b) Cross-sectional view illustrating the scenario-based approach, where multiple candidate locations for the buried toe ($P_2$) are evaluated to identify the optimal rupture depth.

Once the ICS is constructed by the GA-searching process, with the help of the pre-event DEM, the shape and distribution of the released mass is determined for computing the dynamical movement of the landslide body (see Sect. 2.2). To figure out the best-fitted ICS, the criteria are the fitnesses of the reference points on the unburied rupture surface and the deposit surface (the yellow dots in Figure 2).

## 2.2 Dynamic Verification: Run-Out Behavior

Following the generation of candidate rupture surfaces and the determination of the associated displaced volumes, the physical plausibility of each candidate is verified by simulating the subsequent runout behavior. This is achieved using MoSES_2PDF (Modeling on Shallow Flows with Efficient Simulation for Two-Phase Debris Flows), an upgraded version of the simulation tool presented by Ko et al. (2021b).

https://doi.org/10.5194/egusphere-2026-1605
Preprint. Discussion started: 15 June 2026


The model employs a two-phase continuum approach (Wong et al., 2024), treating the landslide mass as a mixture of solid granular material and interstitial fluid. The governing equations are derived in a terrain-following coordinate system which is constructed based on a DEM as given in Tai et al. (2019). When erosion or deposition occurs, a "sub-topography", $\zeta_b$, is introduced to describe the corresponding eroded dimple or deposited heaps. For a detailed derivation of the erosion model and coordinate system formulation, readers are referred to Tai et al. (2019) and Wong et al. (2024) for details.

Figure 3 illustrates the terrain-following coordinate system, where the local tangential directions define the $\xi$- and $\eta$-axes of the terrain-following coordinates, of which the $\zeta$-axis is upwards oriented and normal to the surface. The red surface stands for the evolving local basal surface (sub-topography), denoted by $\zeta_b$, due to erosion and/or deposition processes. The evolution of basal surface is described by

$$\frac{\mathrm{d}\zeta_\mathrm{b}}{\mathrm{d}t} = \frac{\varepsilon^\mathrm{s}}{\phi^\mathrm{s}_\mathrm{b}} = \frac{\varepsilon^\mathrm{f}}{\phi^\mathrm{f}_\mathrm{b}} \quad \text{with} \quad \phi^\mathrm{s}_\mathrm{b} + \phi^\mathrm{f}_\mathrm{b} = 1\,, \tag{1}$$

where $\varepsilon^\mathrm{s}$ and $\varepsilon^\mathrm{f}$ represent the volumetric deposition rates of the solid and fluid phases, respectively, and $\phi^\mathrm{s}$ and $\phi^\mathrm{f}$ are the corresponding volume fractions at the base. Equation $(1)_2$ indicates a fully saturated condition for the entrained/deposited material.

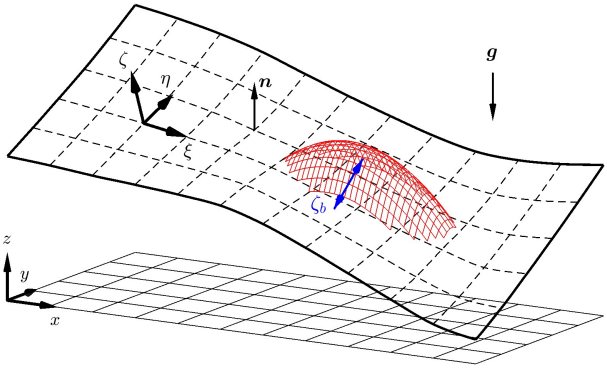


**Figure 3.** Schematic of the smoothed (coordinate) surface with "sub-topography" (deposited heaps).

The feasibility of the two-phase erodible model (Wong et al., 2024) has been explored against outdoor experiments, and the application to the historical 2009 Hsiaolin landslide event is rather successful as well. Hence, the parameter settings for the computation are drawn upon the parameter combinations established by Wong et al. (2024) and the relevant previous works (Tai et al., 2019; Ma et al., 2022; Tai et al., 2023). It should be recalled that the viscosity of the interstitial fluid and the representative grain size play crucial roles in the erosion-deposition mechanism.

The orientation of the reference ellipse has significant impacts on the resulting deposition pattern. In the searching process, there are tens of thousands of ICSs and the associated deposit heaps to be computed, so that a simulation tool with high-computational efficiency is needed. The GPU-accelerated simulation tool (Ko et al., 2021b) is therefore upgraded by integrating the erosion-deposition mechanism, to numerically solve the model equations (Wong et al., 2024). In the original and upgraded MoSES_2PDF, the Nvidia CUDA Toolkit (vers. 11.0 or above) is employed. Regarding the numerical scheme,

https://doi.org/10.5194/egusphere-2026-1605
Preprint. Discussion started: 15 June 2026


the anti-diffusive, non-oscillatory central scheme (adNOC, see Kurganov and Tadmor, 2000; Kurganov and Petrova, 2007; Tai et al., 2019) with Minmod TVD slope limiter is used, while Courant-Friedrichs-Lewy (CFL) number is set by $0.1$ for all the computations in the present study. With the help of the upgraded MoSES_2PDF and benefitting from the GA method (Wang et al., 2022), the duration of the GA-searching process is reduced from several days to tens of minutes in the application examples in Sect 3.

### 2.3 Evaluation Criteria and Optimization Strategy

The fidelity of the approximated rupture surface is quantitatively evaluated by comparing the simulated results against post-event field data derived from the Difference of DEMs (DoD). Two primary quantitative metrics are employed: depth consistency and spatial coverage.

First, the vertical accuracy of the approximated geometry in the erosion zone and the simulated deposit in the accumulation zone is assessed via the Root Mean Square (RMS) error. That is,

$$\mathrm{RMS} = \sqrt{\frac{1}{n}\sum_{i=1}^{n}\left(h^i_{\text{observed}} - h^i_{\text{simulated}}\right)^2}, \tag{2}$$

where $h^i$ represents the depth of erosion or deposition at $n$ selected checking points strategically distributed across both the visible scarp and the deposition area. Second, the horizontal accuracy of the simulated flow path and deposition extent is measured using a Coverage Ratio ($\Lambda_{\text{path}}$). Following the approach of Ko et al. (2021a) and Wang et al. (2022), where a minimum deviation index is utilized to select the most suitable Idealized Curved Surface (ICS), the coverage ratio is calculated based on the Intersection over Union (IoU) concept:

$$\Lambda_{\text{path}} = \frac{A_{\text{sim}} \cap A_{\text{obs}}}{A_{\text{sim}} \cup A_{\text{obs}}} \times 100\%, \tag{3}$$

where $A_{\text{sim}}$ is the simulated area (flow path or deposit) and $A_{\text{obs}}$ is the observed area obtained from post-event orthophotos or DEMs.

## 3 Application To Historical Event

### 3.1 2009 Hsiaolin event

The 2009 Hsiaolin landslide, triggered by heavy rainfall during Typhoon Morakot, is widely regarded as a benchmark event for large-scale landslide research in Taiwan (e.g., Feng, 2011; Kuo et al., 2013; Wu et al., 2014; Tai et al., 2019). With a mobilized area exceeding 250 ha and a failure depth surpassing 80 meters, this catastrophic event generated a comprehensive dataset comprising high-resolution pre- and post-event terrain data. This makes it an ideal case for validating the proposed approximation framework.

Our methodology primarily relies on the GA-ER-ICS framework developed by Wang et al. (2022), and Tai et al. (2020). Traditionally, fitness calculations for estimating landslide depth were based on data collected from on-site inclinometers. However,

https://doi.org/10.5194/egusphere-2026-1605
Preprint. Discussion started: 15 June 2026


many regions prone to large-scale landslides lack such monitoring systems, and the rugged terrain often renders installation impractical, hindering accurate depth measurements. The geometric configuration of the approximation process is visualized in Figures 4 and 5. As shown in Figure 4(a), the orange shaded region delineates the actual landslide scarp, identified from field surveys, and it serves as the ground truth for our approximation.

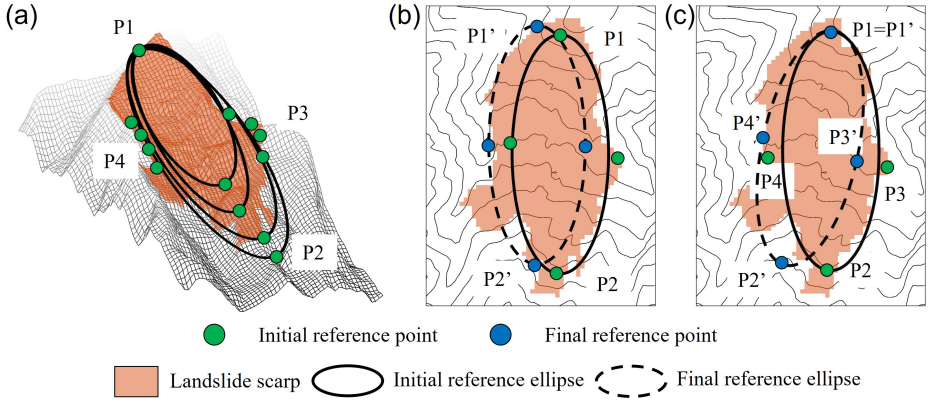


**Figure 4.** Optimization of the reference ellipse orientation. (a) 3D view of the initial ellipses defined by manually selected control points (green) overlaid on the landslide terrain. (b) and (c) Translation and rotation, respectively, during genetic algorithm convergence.

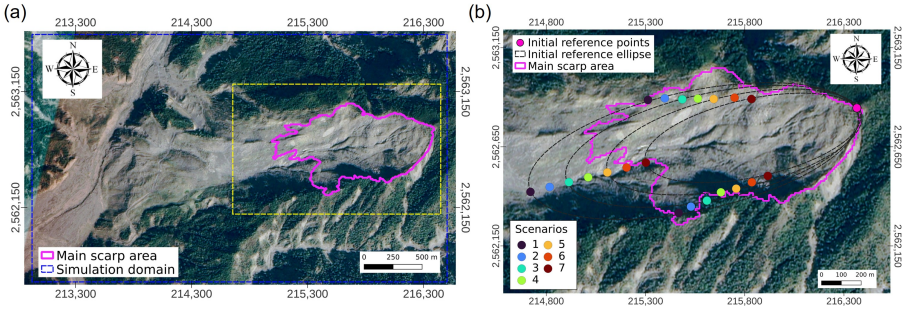


**Figure 5.** Post-event orthophoto of the 2009 Hsiaolin landslide study area. (a) Extent of the main scarp (magenta outline) and the domain for GA evaluation (yellow dashed line). (b) Locations of the initial reference points ($P_1$ to $P_4$). Sources: BIGGIS(https://gis.ardswc.gov.tw/map/, last access: 13 June 2026); basemap: 2010 Formosat-2 Satellite image(2 m) | Powered by QGIS.

Figure 4(b) and (c) illustrate the translation and rotation of the reference ellipse, respectively, f for searching the best-fitted ICS during genetic algorithm convergence, where the green markers ($P_1$ to $P_4$) represent the initial reference points used to define the initial reference ellipse for constructing the corresponding ICS. Figure 5(a) shows the post-event satellite imagery with marking the main scarp (magenta outline) and the evolution domain (yellow dashed line), while panel (b) depicts the locations of the initial reference points ($P_1$ to $P_4$) of the GA-ER-ICS method. The dashed black ellipse indicates the initial reference ellipse generated at the start of the simulation, while the solid black ellipses represent the evolutionary process of

https://doi.org/10.5194/egusphere-2026-1605
Preprint. Discussion started: 15 June 2026


the GA-ER-ICS, eventually converging to the optimal boundary (indicated by the $P_1'$ to $P_4'$) that best fits the topographic depression.

Tang et al. (2020) has attempted to estimate the landslide volumes by comparing numerical terrain data from pre- and post-event conditions. However, their approach may not be applicable when displaced materials have not fully cleared the rupture surface. Although the locations of erosion additional points were compared in their study, the optimal quantity and density of reference points within the landslide surface scarp were not investigated. In the case of the 2009 Hsiaolin Village landslide, the displaced materials had completely slid downstream, making their method (Tang et al., 2020), i.e., constructing erosion additional points, particularly relevant for our study. Therefore, this study explores different intervals of erosion additional points (HS-1 to HS-5) within the known landslide surface area. The estimated probable landslide surface of rupture and the corresponding sediment transport flow path were then compared with the results from Tai et al. (2020). To assess the suitability of the GA-ER-ICS for the starting reference points scenario proposed in this study, a series of randomly generated erosion additional points were placed within the main landslide scarp area. The designed erosion additional points (shown as yellow dots in Figure 6) included various grid spacings: 2 (HS-1), 10 (HS-2), 20 (HS-3), 30 (HS-4), and 40 (HS-5) grids, which served as the comparison cases in this study. The candidate rupture surfaces generated from these scenarios were first screened based on geometric fit. As summarized in Figure 6, candidates were filtered by an RMS error threshold of 15.0 m and a coverage threshold of 70%. Two representative scenarios, HS-3 (sc-5) and HS-5 (sc-4), were selected for dynamic verification by using two-phase grain-fluid model which the parameters used in simulation are same as Tai et al. (2019) and listed in Table 2.

The decisive validation is provided by the dynamic simulation of the subsequent runout, as visually depicted in Figure 7. regarding the deposition depth (Panels c versus d), both scenarios satisfactorily reproduce the general accumulation pattern within the valley, showing reasonable agreement with the major deposit zones. However, a critical distinction emerges from the overlay analysis of the flow paths (Panels e versus f). In these panels, the cyan regions signify the "True Positive" area where the simulation successfully overlaps with the actual landslide path, whereas the yellow and blue/pink regions represent "False Negatives" (observed but missed) and "False Positives" (simulated but not observed), respectively.

A comparative examination of Figure 7(e) and (f) reveals that Scenario HS-3 (left column) generates a significantly larger cyan overlap area ($\Lambda_{\text{path}} = 80.24\%$) compared to HS-5 (right column), which achieves only 68.32%. Notably, the extensive yellow areas visible at the distal end of the flow in the HS-5 results indicate that the model significantly underestimated the runout distance. This visual evidence confirms that while HS-5 appeared geometrically valid during the initial scarp analysis, it failed to capture the sufficient kinematic energy required to drive the flow to its actual historical extent.

### 3.2 2022 Provincial Highway 7 (86.5K) event

To assess the applicability of the proposed framework to a recent event with a buried toe, we investigated the landslide that occurred at the 86.5 km mark of Provincial Highway No. 7 in Yilan, Taiwan, on October 16, 2022. Triggered by Typhoon Nesat, which brought an accumulated rainfall of 1,112 mm within 62 hours, the slope failure destroyed approximately 400 meters of the roadway.

https://doi.org/10.5194/egusphere-2026-1605
Preprint. Discussion started: 15 June 2026


**Table 2.** Parameter values used in simulations

| | 2009 Hsiaolin Event | 2022 Provincial Highway No. 7 Event | Description |
|---|---|---|---|
| $\rho^f/\rho^s$ | 1.42/2.60 | 1.42/2.60 | Density ratio |
| $\phi^{s0}$ | 0.5 | 0.5 | Initial solid concentration |
| $\delta_b$ | 16° | 35° | Angle of basal friction (solid phase) |
| $\vartheta_b^f$ | 5.0 | 5.0 | Navier fluid friction coefficient |
| $c_D$ | 6.0 | 6.0 | Drag coefficient |
| $\mu^{\mathrm{f}}$ | 0.5245 Pa·s | 0.5245 Pa·s | Viscosity of interstitial fluid |
| $N_R$ | 268 | 268 | Viscous number |
| $d$ | 0.5 m | 0.2 m | Sediment median diameter |
| $\tilde{\Psi}_{\mathrm{th}}^{\mathrm{non}}$ | 0.054 | 0.054 | Threshold value of Shields parameter |
| $\tilde{v}_{\mathrm{lim}}^{\mathrm{non}}$ | 1.6 | 1.8 | Non-dimensional critical speed for deposit |
| $\tilde{\Sigma}_{\mathrm{lim}}^{\mathrm{non}}$ | 0.016 | 0.018 | Threshold value for deposit |
| $\phi_{\mathrm{b}}^{\mathrm{f}}$ | 0.38 | 0.38 | Porosity of bottom |
| $\alpha_{\mathrm{E}}$ | 0.00008 | 0.000025 | Entrainment coefficient |
| $\alpha_{\mathrm{D}}$ | 0.04 | 0.07 | Deposition coefficient |
| $n$ | 0.03 s/m$^{1/3}$ | 0.03 s/m$^{1/3}$ | Manning coefficient |
| $\Delta x = \Delta y$ | 10.0 m | 1.0 m | Mesh size |
| CFL | 0.1 | 0.1 | CFL number |

High-resolution Digital Surface Models (DSMs) were generated via post-event UAV photogrammetry surveys. The Difference of DEMs (DoD) was subsequently derived using the post-event and pre-event LiDAR-derived DEMs (both at 1 m resolution). As illustrated in Figure 8(a), the DoD clearly indicates the deposition area (positive elevation change, indicating displaced material) and the source zone (negative elevation change). The red boundary delineates the assessed endangered area, defined by elevation changes exceeding $\pm 0.1$ m. This DoD serves as the ground truth for validating our approximation (yellow dots).

Applying the findings from the 2009 Hsiaolin case study, where a moderate density of control points was found sufficient, we adopted a sparse configuration for the GA-ER-ICS. Approximately 24 erosion control points (yellow dots in Figure 8(a)) were generated with a grid spacing of 70 pixels within the potential scarp area identified from orthophotos (magenta outline).

Figure 8(b) shows the reconstruction process tested various scenarios regarding the location of the rupture toe ($P_2$), which is critical for buried-toe landslides. The GA-ER-ICS simulations revealed a distinct trend, which indicators of fitness (RMS and coverage) improved significantly when the initial reference point $P_2$ was set closer to the existing highway platform, rather than

https://doi.org/10.5194/egusphere-2026-1605
Preprint. Discussion started: 15 June 2026


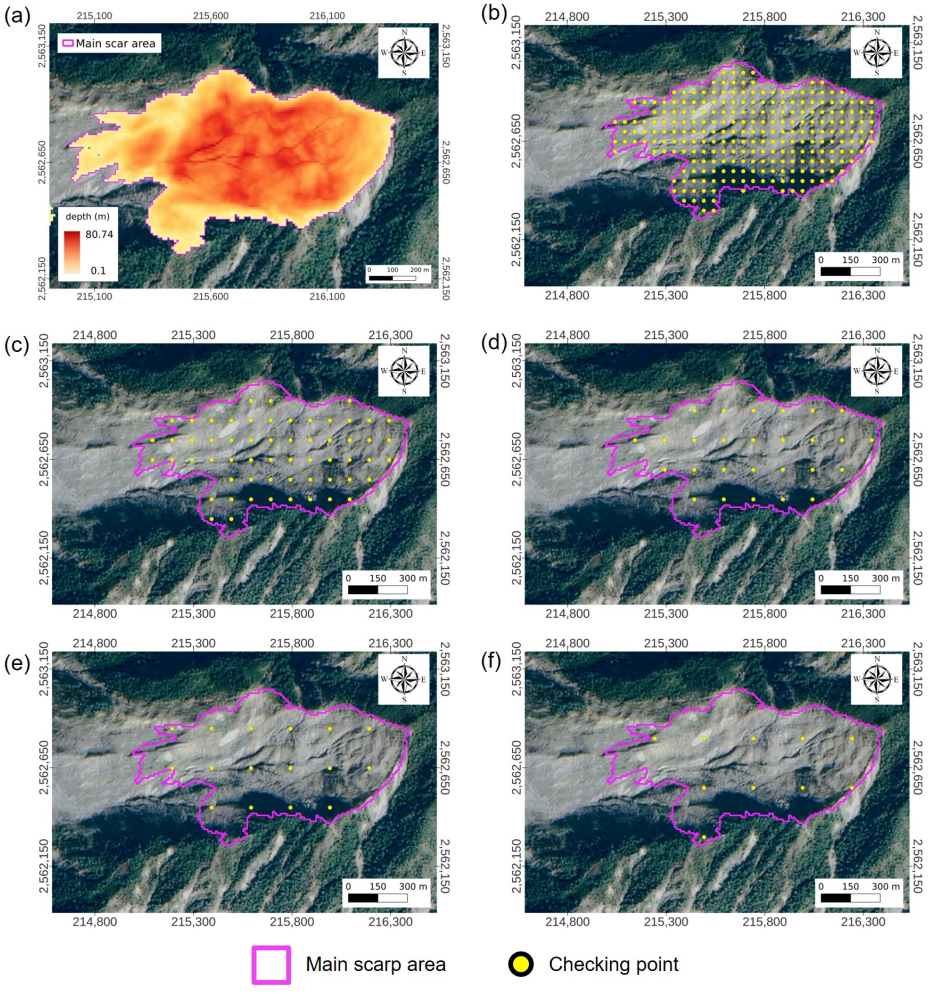


**Figure 6.** Configuration of erosion control points with varying sampling resolutions. (a) The calculated erosion depth of the landslide scarp used as the ground truth. (b) Scenario HS-1: High-density sampling (2-grid spacing). (c)–(f) Scenarios HS-2 to HS-5: Progressively sparser distributions with grid spacings of 10, 20, 30, and 40, respectively. Sources: BIGGIS(https://gis.ardswc.gov.tw/map/, last access: 13 June 2026); basemap: 2010 Formosat-2 Satellite image(2 m) | Powered by QGIS.

near the landslide crown. This suggests that the rupture surface likely extends deep into the slope, with the toe buried near the river bank below the highway. Based on the screening criteria established in the previous section (RMS $< 5.5$ m and Coverage $> 65.0\%$), Scenarios 2 and 3 were selected as the most plausible candidates for dynamic verification. The approximated depth distributions for these scenarios are presented in Figure 8(c) and (d).

The selected scenarios were subjected to dynamic simulation using MoSES_2PDF. The rheological parameters, including a basal friction angle of $\delta_b = 35°$, were assigned based on the mixture composition and the classification by Scheidegger Scheidegger (1973), as detailed in Table 2. The simulation results are summarized in Table 3 and visualized in Figure 8. A comparison

https://doi.org/10.5194/egusphere-2026-1605
Preprint. Discussion started: 15 June 2026


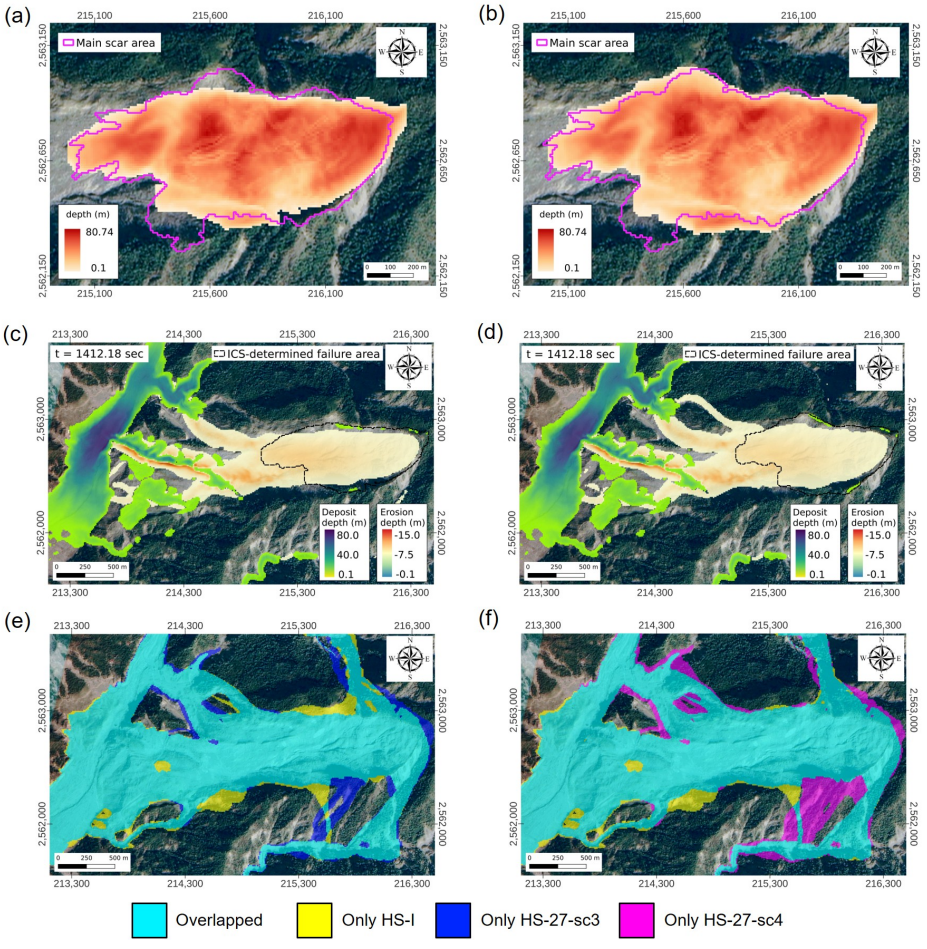


**Figure 7.** Flow paths computed using the approximated rupture surfaces. The left column corresponds to Scenario HS-3 (moderate point density), and the right column to Scenario HS-5 (low point density). (a)–(b) approximated failure depth distributions. (c)–(d) Simulated final deposition depths at $t = 1412$ s. (e)–(f) Cyan areas indicate overlapping regions, while yellow and blue/pink areas represent regions covered only in a single scenario. Sources: BIGGIS(https://gis.ardswc.gov.tw/map/, last access: 13 June 2026); basemap: 2010 Formosat-2 Satellite image(2 m) | Powered by QGIS.

of the mobilized volumes reveals that Scenario 2 overestimated the volume by 8.1%, while Scenario 3 underestimated it by 15.4% relative to the DoD-derived volume (682,824 $m^3$). This discrepancy highlights the inherent uncertainty in reconstructing a buried rupture surface solely from surface evidence.

Despite these volumetric deviations, the simulated flow exhibits robust kinematic behavior:

**Deposition Depth**: The RMS errors for the deposition depth in Scenarios 2 and 3 were 8.63 m and 8.62 m, respectively. This represents a marginal increase of approximately 0.33 m compared to the simulation driven by the actual DoD (RMS = 8.29 m).

https://doi.org/10.5194/egusphere-2026-1605
Preprint. Discussion started: 15 June 2026


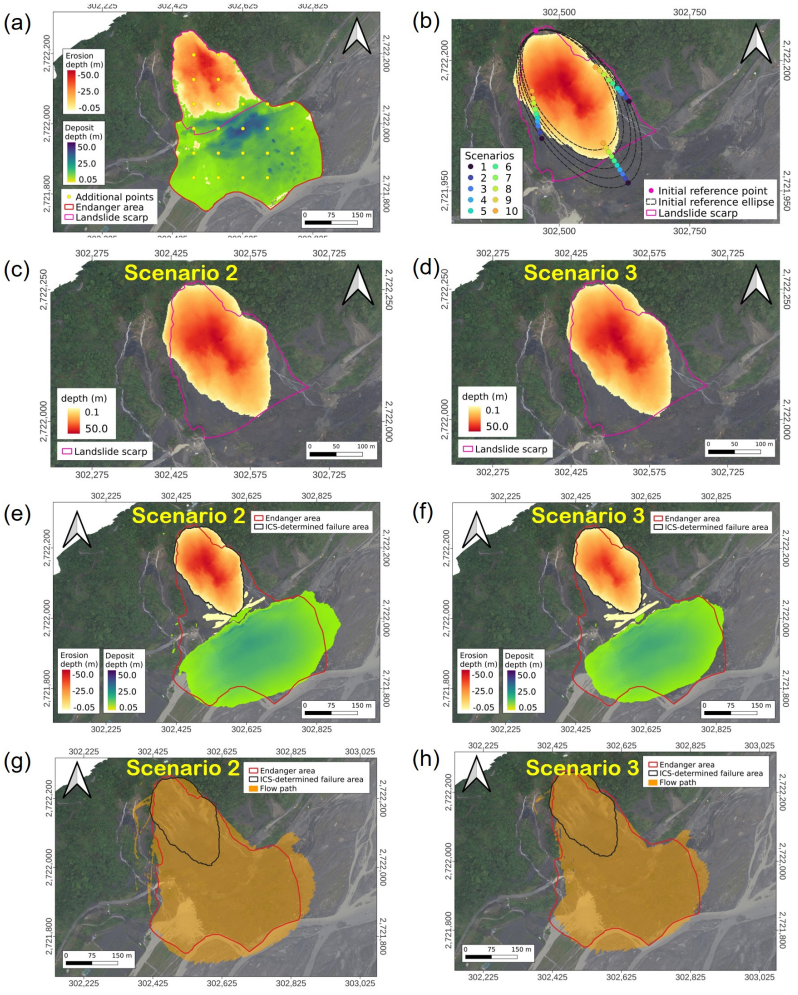


**Figure 8.** Application to the 2022 Provincial Highway No. 7 landslide event. (a) Spatial distribution of erosion (source) and deposition areas derived from the DoD, with checking points (yellow dots) generated for fitness evaluation. (b) Visualization of the initial reference ellipses and the evolutionary search process for the buried toe. (c)–(d) Inferred landslide depths for the two best-fit scenarios (Scenario 2 and 3). (e)–(f) Simulated final deposit distribution corresponding to the approximated volumes. (g)–(h) Comparison of the modeled flow paths (orange areas, flow depth $> 0.1$ m) against the actual hazard zone (red outline), demonstrating the model's capability in delineating the impact area.

This slight degradation in vertical accuracy is expected given the synthetic nature of the rupture surface but remains within an acceptable range for hazard scoping.

**Flow Path Coverage**: Most importantly, the spatial extent of the hazard zone was well-captured. As shown in Figure 8(g) and (h), the predicted flow paths (orange areas) closely align with the actual hazard boundary (red line). Scenario 3 achieved a path coverage ($\Lambda_{\text{path}}$) of 84.28%, which is effectively identical to the reference run (83.96%).

https://doi.org/10.5194/egusphere-2026-1605
Preprint. Discussion started: 15 June 2026


**Table 3.** Result of estimation with evaluating indicator additional point of erosion and deposit

| | Landslide distribution | | | Deposit distribution | |
|---|---|---|---|---|---|
| Scenario | RMS | coverage(%) | volume ($m^3$) | RMS | coverage(%) |
| actual DoD | —- | —— | 682,824 | 8.29 | 83.96 |
| 2 | 4.62 | 65.29 | 738,000 | 8.63 | 78.78 |
| 3 | 5.45 | 65.11 | 577,500 | 8.62 | 84.28 |

These results indicate that, even with a volumetric uncertainty of up to 15%, the proposed GA-ER-ICS framework can reliably delineate the potential impact area. This robustness suggests that, for preliminary hazard assessment in data-scarce regions where the toe of the landslide is buried, the proposed method offers a viable alternative to complex geotechnical investigations.

## 4 Discussion

The two case studies presented in Section 3 demonstrate that coupling the GA-ER-ICS geometric search with the MoSES_2PDF dynamic solver can effectively reduce the indeterminacy inherent to buried-toe landslides. To facilitate the broader use of the proposed framework and to be transparent about its operating envelope, this section discusses (i) the range of landslide settings in which the framework is expected to perform robustly, (ii) its scalability with respect to event magnitude and computational cost, (iii) its principal limitations, and (iv) the data conditions required for transferring the workflow to other regions. A concise comparison with existing rupture-surface estimation methods is also provided to position the framework within the broader literature.

### 4.1 Broader applicability across landslide types and settings

The proposed framework is specifically designed for landslides in which (a) a clear scarp can be delineated from the post-event topography or orthophoto, (b) the displaced material remains within an identifiable deposition zone, and (c) the rupture surface can be reasonably approximated by a single, smoothly curved surface. These conditions are characteristic of rotational and translational landslides in the sense of Varnes (1978) and Hungr et al. (2014), which constitute the great majority of buried-toe failures encountered in post-disaster forensic investigations.

For other failure types, the applicability of the framework is more restricted. Rockfalls, topples, and debris avalanches that fragment severely during transport are not well represented by an idealized curved rupture surface, and the assumption of a single coherent release mass underlying MoSES_2PDF becomes less valid. Multi-stage or retrogressive failures, in which several discrete rupture surfaces develop sequentially, would in principle require the GA-ER-ICS to be applied independently to each stage; this remains an open avenue for further work. The two cases analysed in present study, which the 2009 Hsiaolin event (a deep-seated, large-volume failure on weathered sedimentary rock) and the 2022 Provincial Highway No. 7 event (a

https://doi.org/10.5194/egusphere-2026-1605
Preprint. Discussion started: 15 June 2026


comparatively shallow road-cut failure), both fall within the rotational-translational category and were triggered by rainfall. For seismically triggered events, the same geometric search procedure should be applicable, but the rheological parameters listed in Table 2, in particular the basal friction angle $\delta_b$ and the entrainment and deposition coefficients $\alpha_{\mathrm{E}}$ and $\alpha_{\mathrm{D}}$, would need to be re-calibrated for the local geological context. Likewise, applications in volcanic, glacial, or permafrost settings are expected to require adjustments to the constitutive description of the granular-fluid mixture.

### 4.2 Scalability with event magnitude and computational cost

The two presented events differ by nearly two orders of magnitude in mobilised volume (approximately $2.0 \times 10^7$ m$^3$ for Hsiaolin versus $6.83 \times 10^5$ m$^3$ for the Provincial Highway No. 7 event), and by an order of magnitude in computational mesh resolution (10 m versus 1 m; see Table 2). The framework converged to physically plausible solutions in both cases, suggesting reasonable robustness across the size range commonly encountered in regional hazard assessment. At the lower end of the size spectrum (small, shallow landslides with volumes below $\sim 10^4$ m$^3$), the ellipsoidal ICS assumption may become coarse relative to the actual rupture geometry, and the empirical area–volume relations cited in Section 2.1 (Guzzetti et al., 1999; Larsen et al., 2010; Meier et al., 2020) may provide an equally informative first estimate of volume with much lower computational effort. At the upper end, for very large debris flows events with volumes exceeding $10^8$ m$^3$, the depth-averaged shallow-water assumption underlying MoSES_2PDF becomes less appropriate, and full three-dimensional or hybrid models may be preferable for dynamic verification.

In terms of computational cost, the combined GA-ER-ICS plus MoSES_2PDF workflow benefits from the GPU implementation of both components, yielding a reported speed-up of more than two orders of magnitude over CPU-based serial computation (Ko et al., 2021b; Wang et al., 2022). In the case studies, the complete search for the best-fitted ICS, including the evaluation of all candidate surfaces and the associated dynamic simulations was reduced from several days on conventional hardware to a few tens of minutes on a single workstation equipped with a contemporary Nvidia GPU. This computational efficiency is what makes scenario-based exploration of the buried toe location operationally feasible, and is therefore essential to the practical value of the framework rather than merely a technical convenience.

### 4.3 Limitations

Several limitations of the present framework should be acknowledged. First, the rupture surface is parameterised as an idealised ellipsoidal ICS. While the genetic algorithm allows substantial flexibility in orientation, eccentricity, and depth, this parameterisation cannot represent strongly compound rupture surfaces, failures controlled by pre-existing discontinuities (e.g. bedding planes or major joints), or surfaces with multiple local minima in depth. In such cases the framework will still return a best-fitting ellipsoidal surface, but the geological realism of the result will degrade.

Second, dynamic verification reduces but does not eliminate the indeterminacy associated with the buried toe. As shown in Section 3.2, even after screening by RMS error and coverage and after dynamic simulation, the inferred volume of the 2022 Provincial Highway No. 7 event still bracketed the DoD-derived reference value by between $-15.4\%$ and $+8.1\%$. A useful operational corollary of the present results is that the framework appears to constrain the impact footprint much more tightly

https://doi.org/10.5194/egusphere-2026-1605
Preprint. Discussion started: 15 June 2026


than it constrains the mobilised volume: the path coverage $\Lambda_{\text{path}}$ remained above 80% across plausible scenarios, whereas volume estimates varied by more than 20% across the same set. Users of the framework should therefore treat the inferred volume as an interval estimate rather than a single best value.

Third, the framework requires both pre- and post-event DEMs of comparable quality, together with an orthophoto or equivalent imagery from which the scarp boundary can be delineated. In situations where only post-event data are available. For example, in remote regions without prior LiDAR or photogrammetric coverage, the proposed workflow cannot be applied directly. Likewise, the rheological parameters listed in Table 2 were drawn from prior calibrations on Taiwan events (Tai et al., 2019; Wong et al., 2024); for applications in new geological provinces, an initial parameter sensitivity study is advisable.

Fourth, the present implementation assumes a single, instantaneous release of the entire rupture mass. Progressive failures, secondary mobilisation following the initial collapse, or rainfall-driven entrainment occurring after the main event are not represented and would require additional model components.

### 4.4 Transferability and recommended data conditions

Based on the two case studies, a tentative set of data conditions can be proposed under which the framework is expected to perform robustly. Pre- and post-event DEMs at a horizontal resolution finer than approximately one tenth of the longest landslide dimension appear to be sufficient, in the Hsiaolin case a 10 m DEM was adequate for an event spanning more than 1 km, whereas the smaller Provincial Highway No. 7 event required a 1 m DEM to resolve the scarp. The sensitivity analysis on the Hsiaolin event further indicates that approximately 16 erosion control points (a $4 \times 4$ grid) within the visible scarp are sufficient for the GA to converge on a physically realistic rupture surface; denser sampling did not yield materially better solutions, while substantially sparser sampling (HS-5, 40-grid spacing) produced surfaces that were geometrically acceptable but kinematically incorrect, as evidenced by the underestimated runout in Figure 7(f).

Transferring the framework to a new region therefore requires, at minimum: (i) pre- and post-event DEMs at compatible resolution and co-registered to a common datum; (ii) a post-event orthophoto or comparable imagery enabling delineation of the scarp and deposition zone; (iii) an initial estimate of the released volume, either from local DoD analysis or from regional area with volume scaling relations (Larsen et al., 2010; Meier et al., 2020); and (iv) an indicative range for the basal friction angle and grain size representative of the local geology. Where the latter are uncertain, a small ensemble of dynamic simulations spanning plausible parameter ranges can be carried out within the same GPU-accelerated framework without prohibitive computational overhead.

### 4.5 Positioning within existing approaches

The distinguishing feature of the present framework, relative to the methods listed in Table 1, is the explicit use of post-failure kinematics as an inverse constraint on the rupture geometry. Purely geometric methods such as SLBL (Jaboyedoff et al., 2012), SMS (Kuo et al., 2020), and polynomial surface fitting (Tang et al., 2020) infer the rupture surface from topographic continuity alone, and consequently cannot distinguish between geometrically similar surfaces that would produce markedly different runout behaviour. Limit-equilibrium and stability-based methods (GEO-SLOPE, 2021; Reid et al., 2015) introduce mechanical

https://doi.org/10.5194/egusphere-2026-1605
Preprint. Discussion started: 15 June 2026


constraints but require subsurface material properties (cohesion, friction angle, pore pressure) that are rarely available immediately after a disaster. The proposed framework requires only surface observables (DEMs and orthophotos) and a representative rheology, and is therefore complementary to existing methods: it can be used as a rapid first-pass tool in the immediate aftermath of an event, with the resulting rupture surface subsequently refined by limit-equilibrium analysis once subsurface data become available.

## 5 Conclusions

This study presents an integrated computational framework for reconstructing the rupture surface of landslides where the toe is buried, which a common yet challenging scenario in post-disaster forensics. By coupling the geometric search capability of the GA-ER-ICS with the dynamic verification provided by the GPU-accelerated MoSES_2PDF model, we have established a methodology that constrains the infinite geometric possibilities of a buried slip surface through physical kinematic evidence.

A pivotal advantage of the proposed framework is its computational efficiency. The implementation of both the genetic algorithm and the two-phase flow solver on CUDA-GPU architecture yields a speedup of over 100 times compared to conventional CPU-based serial computing (Ko et al., 2021b; Wang et al., 2022). This efficiency is not merely a technical improvement; it transforms the reconstruction process from a time-consuming research task into a viable operational routine. It allows for the rapid testing of hundreds of geometric scenarios within minutes, requiring only fundamental pre- and post-event DEMs and orthophotos, thus minimizing the dependency on costly and often unavailable geotechnical subsurface data.

The application to the 2009 Hsiaolin landslide provided critical insights into data requirements. The sensitivity analysis demonstrated that a high density of erosion control points is not strictly necessary; a moderate random distribution (approximately 16 points or a $4 \times 4$ grid) is sufficient for the GA to converge to a physically realistic rupture surface. This finding significantly lowers the barrier for applying this method to events with limited topographic data.

The validation against the 2022 Provincial Highway No. 7 event highlighted the framework's robustness for hazard mapping. Although the approximated landslide volume exhibited deviations of up to 15% due to the inherent indeterminacy of the buried toe, the subsequent dynamic simulations proved highly resilient. The predicted deposition depths showed marginal RMS increases (+0.34 m), and crucially, the predicted hazard zones achieved coverage rates exceeding 80% compared to the ground truth. This indicates that even when the exact rupture geometry is approximated, the coupled dynamic model can reliably delineate the potential impact area.

As discussed in Section 4, the framework is best suited to rotational and translational landslides in which the rupture surface can be reasonably approximated by a single smoothly curved surface, and it requires both pre- and post-event DEMs together with a delineateable scarp boundary. Within these operating conditions, the integration of an idealized geometric search with physics-based flow modeling offers a powerful tool for backward analysis. This approach successfully bridges the gap between static geometric fitting and dynamic runout simulation. It provides engineers and researchers with a quick-scanning capability to assess potential failure scenarios and impact zones in the immediate aftermath of a disaster, particularly in regions where complex geological investigations are not immediately feasible. Future work will focus on extending the parameterization

https://doi.org/10.5194/egusphere-2026-1605
Preprint. Discussion started: 15 June 2026


to compound rupture surfaces and on coupling the framework with rainfall-driven hydrological forcing to support pre-event hazard scenarios in addition to post-event back-analysis.

*Author contributions.* Conceptualization: Y.-C.T. and H.-K.W.; methodology: Y.-C.T.; software: Y.-C.T. and H.-K.W.; validation: L.-C.F., H.-K.W. and Y.-C.T.; formal analysis: L.-C.F., Y.-C.T. and H.-K.W.; investigation: L.-C.F. and Y.-C.T.; resources: Y.-C.T.; data curation: L.-C.F. and H.-K.W.; writing-original draft preparation: H.-K.W. and Y.-C.T.; writing-review and editing: Y.-C.T.; visualization: H.-K.W.; supervision: Y.-C.T.; project administration: Y.-C.T.; funding acquisition: Y.-C.T.

*Competing interests.* The contact author has declared that none of the authors has any competing interest.

*Code and data availability.* The executable code of MoSES_2PDF, the processed datasets supporting the figures, and the GA-ER-ICS convergence histories are available from the corresponding author upon reasonable request. The Digital Elevation Models (DEMs) as well as the UAV-derived post-event Digital Surface Model (DSM) for the 2022 Provincial Highway No. 7 event, were provided by Dr. C.F. Lee and are also available from the corresponding author upon reasonable request, subject to the data provider's restrictions.

*Acknowledgements.* This research was founded by the National Science and Technology Council, Taiwan (NSTC 112-2221-E-006-051-MY3).

https://doi.org/10.5194/egusphere-2026-1605
Preprint. Discussion started: 15 June 2026


## References

Terzaghi, K.: Mechanism of landslides. Publishing House: Geological Society of America, Inc., 1950.

Jaboyedoff, M., Michoud, C., Derron, M.-H., Voumard, J., Leibundgut, G., Sudmeier-Rieux, K., Nadim, F., Leroi, E.: Human-induced landslides: toward the analysis of anthropogenic changes of the slope environment. Landslides and engineered slopes. Experience, theory and practice, 217–232, 2018.

Legros, F., Cantagrel, J.-M., Devouard, B.: Pseudotachylyte (frictionite) at the base of the Arequipa volcanic landslide deposit (Peru): Implications for emplacement mechanisms. The Journal of Geology, 108, 604–611, https://doi.org/10.1086/314421, 2000.

Hsu, K.J.: Catastrophic debris streams (Sturzstroms) generated by rockfalls. Geological Society of America Bulletin, 86, 129–140, https://doi.org/10.1130/0016-7606(1975)86<129:CDSSGB>2.0.CO;2, 1975.

Varnes, D.J.: Slope movement types and processes. Special Report, 176, 11–33, 1978.

Hungr, O., Leroueil, S., Picarelli, L.: The Varnes classification of landslide types, an update. Landslides, 11, 167–194, https://doi.org/10.1007/s10346-013-0436-y, 2014.

Scheidegger, A.E.: On the prediction of the reach and velocity of catastrophic landslides. Rock Mechanics, 5, 231–236, https://doi.org/10.1007/BF01301796, 1973.

Corominas, J.: The angle of reach as a mobility index for small and large landslides. Canadian Geotechnical Journal, 33, 260–271, https://doi.org/10.1139/t96-005, 1996.

Jakob, M.: A size classification for debris flows. Engineering Geology, 79, 151–161, https://doi.org/10.1016/j.enggeo.2005.01.006, 2005.

Jakob, M., Stein, D., Ulmi, M.: Vulnerability of buildings to debris flow impact. Natural Hazards, 60, 241–261, https://doi.org/10.1007/s11069-011-0007-2, 2012.

von Ruette, J., Lehmann, P., Or, D.: Linking rainfall-induced landslides with predictions of debris flow runout distances. Landslides, 13, 1097–1107, https://doi.org/10.1007/s10346-015-0621-2, 2016.

Jaboyedoff, M., Carrea, D., Derron, M.-H., Oppikofer, T., Penna, I.M., Rudaz, B.: A review of methods used to estimate initial landslide failure surface depths and volumes. Engineering Geology, 267, 105478, https://doi.org/10.1016/j.enggeo.2020.105478, 2020.

Travelletti, J., Malet, J.-P., Delacourt, C.: Image-based correlation of Laser Scanning point cloud time series for landslide monitoring. International Journal of Applied Earth Observation and Geoinformation, 32, 1–18, https://doi.org/10.1016/j.jag.2014.03.022, 2014.

Tang, C., Tang, J., van Westen, C.J., Han, J., Mavrouli, O., Tang, C.: Modeling landslide failure surfaces by polynomial surface fitting. Geomorphology, 368, 107358, https://doi.org/10.1016/j.geomorph.2020.107358, 2020.

Jaboyedoff, M., Oppikofer, T., Abellán, A., Derron, M.-H., Loye, A., Metzger, R., Pedrazzini, A.: Use of LIDAR in landslide investigations: a review. Natural Hazards, 61(1), 5–28, https://doi.org/10.1007/s11069-010-9634-2, 2012.

Kuo, C.Y., Tsai, P.W., Tai, Y.C., Chan, Y.H., Chen, R.F. and Lin, C.W.: Application assessments of using scarp boundary-fitted, volume constrained, smooth minimal surfaces as failure interfaces of deep-seated landslides. Frontiers in Earth Science, 211, https://doi.org/10.3389/feart.2020.00211, 2020.

GEO-SLOPE International Ltd. Stability Modeling with GeoStudio (version 6th), 2021.

Reid, M.E., Christian, S.B., Brien, D.L., Henderson, S.T.: Scoops3D: software to analyze 3D slope stability throughout a digital landscape. US Geological Survey, 14, A1, https://doi.org/10.3133/tm14A1, 2015.

https://doi.org/10.5194/egusphere-2026-1605
Preprint. Discussion started: 15 June 2026


Brunner, G.W.: HEC-RAS river analysis system: hydraulic reference manual, version 5.0. US Army Corps of Engineers-Hydrologic Engineering Center, https://www.hec.usace.army.mil/software/hec-ras/documentation/HEC-RAS%205.0%20Reference%20Manual.pdf(last access: 20 March 2026), February 2016.

Nakatani, K., Wada, T., Satofuka, Y., Mizuyama, T.: Development of "Kanako 2D (Ver. 2.00)", a user-friendly one- and two-dimensional debris flow simulator equipped with a graphical user interface. International Journal of Erosion Control Engineering, 1, 62–72, https://doi.org/10.13101/ijece.1.62, 2008.

WSL Institute for Snow and Avalanche Research SLF. RAMMS: DEBRISFLOW User Manual (v1.8.0), https://ramms.ch/wp-content/uploads/RAMMS_DBF_Manual.pdf (last access: 20 March 2026), July 2024.

Tai, Y.C., Heß, J., Wang, Y.: Modeling two-phase debris flows with grain-fluid separation over rugged topography: Application to the 2009 Hsiaolin Event, Taiwan. Journal of Geophysical Research: Earth Surface, 124, 305–333, https://doi.org/10.1029/2018JF004671, 2019.

Wang, C.L., Ko, C.J., Wong, H.K., Pai, P.H., Tai, Y.C.: An approach for preliminary landslide scarp assessment with genetic algorithm (GA). Water, 14, 2400, https://doi.org/10.3390/w14152400, 2022.

Tai, Y.C., Ko, C.J., Li, K.D., Wu, Y.C., Kuo, C.Y., Chen, R.F., Lin, C.W.: An idealized landslide failure surface and its impacts on the traveling paths. Frontiers in Earth Science, 313, https://doi.org/10.3389/feart.2020.00313, 2020.

Ko, C.J., Wang, C.L., Wong, H.K., Lai, W.C., Kuo, C.Y., Tai, Y.C.: Landslide Scarp Assessments by Means of an Ellipse-Referenced Idealized Curved Surface. Frontiers in Earth Science, 9, 733413, https://doi.org/10.3389/feart.2021.733413, 2021.

Wong, H.K., Tai, Y.C., Tsunetaka, H., Hotta, N.: Two-phase approach to modeling the grain-fluid flows with deposition and entrainment over rugged topography. Advances in Water Resources, 104691, https://doi.org/10.1016/j.advwatres.2024.104691, 2024.

Guzzetti, F., Carrara, A., Cardinali, M., Reichenbach, P.: Landslide hazard evaluation: a review of current techniques and their application in a multi-scale study, Central Italy. Geomorphology, 31, 1–4, 181–216, https://doi.org/10.1016/S0169-555X(99)00078-1, 1999.

Larsen, I.J., Montgomery, D.R., Korup, O.: Landslide erosion controlled by hillslope material. Nature Geoscience, 3(4), 247–251, https://doi.org/10.1038/ngeo776, 2010.

Guzzetti, F., Ardizzone, F., Cardinali, M., Galli, M., Reichenbach, P., Rossi, M.: Distribution of landslides in the Upper Tiber River basin, central Italy. Geomorphology, 96(1–2), 105–122, https://doi.org/10.1016/j.geomorph.2007.07.015, 2008.

Guzzetti, F., Ardizzone, F., Cardinali, M., Rossi, M., Valigi, D.: Landslide volumes and landslide mobilization rates in Umbria, central Italy. Earth and Planetary Science Letters, 279(3-4), 222-229, https://doi.org/10.1016/j.epsl.2009.01.005, 2009.

Meier, C., Jaboyedoff, M., Derron, M.-H., Gerber, C.: A method to assess the probability of thickness and volume estimates of small and shallow initial landslide ruptures based on surface area. Landslides, 17(4), 975–982, https://doi.org/10.1007/s10346-020-01347-0, 2020.

Ko, C.J., Chen, P.C., Wong, H.K., Tai, Y.C.: MoSES_2PDF: A GIS-compatible GPU-accelerated high-performance simulation tool for grain-fluid shallow flows. arXiv [preprint], arXiv:2104.06784, https://doi.org/10.48550/arXiv.2104.06784, April 2021.

Ma, C.Y., Ko, C.J., Wong, H.K., Tai, Y.C.: Modeling Three-Phase Debris Flows in Terrain-Following Coordinate System and Its GPU Computation with CUDA Structure. Journal of the Chinese Institute of Civil and Hydraulic Engineering, 34, 7, 597–604, https://doi.org/10.6652/JoCICHE.202211_34(7).0004, 2022.

Tai, Y.C., Wong, H.K., Ma, C.Y.: A Simplex Multi-Phase Approach for Modelling Debris Flows in Smoothed-Terrain-Following Coordinate System. E3S Web of Conferences, 415, 02022, https://doi.org/10.1051/e3sconf/202341502022, 2023.

Kurganov, A., Tadmor, E.: New high-resolution central schemes for nonlinear conservation laws and convection–diffusion equations. Journal of Computational Physics, 160, 1, 241–282, https://doi.org/10.1006/jcph.2000.6459, 2000.

https://doi.org/10.5194/egusphere-2026-1605
Preprint. Discussion started: 15 June 2026


Kurganov, A., Petrova, G.: A second-order well-balanced positivity preserving central-upwind scheme for the Saint-Venant system. Communications in Mathematical Sciences, 5, 1, 133–160, https://doi.org/10.4310/cms.2007.v5.n1.a6, 2007.

Feng, Z.: The seismic signatures of the 2009 Shiaolin landslide in Taiwan. Natural Hazards and Earth System Sciences, 11, 1559–1569, https://doi.org/10.5194/nhess-11-1559-2011, 2011.

Kuo, Y.S., Tsai, Y.J., Chen, Y.S., Shieh, C.L., Miyamoto, K., Itoh, T.: Movement of deep-seated rainfall-induced landslide at Hsiaolin Village during Typhoon Morakot. Landslides, 10, 191–202, https://doi.org/10.1007/s10346-012-0315-y, 2013.

Wu, C.H., Chen, S.C., Feng, Z.Y.: Formation, failure, and consequences of the Xiaolin landslide dam, triggered by extreme rainfall from Typhoon Morakot, Taiwan. Landslides, 11, 357–367, https://doi.org/10.1007/s10346-013-0394-4, 2014.